Nanoscale

PAPER

View Article Online
View Journal | View Issue

Cite this: *Nanoscale*, 2023, **15**, 2162

Voltage driven chemiresistor with ultralow power consumption based on self-heating bridged WO_3 nanowires†

Tiantian Dai,[a,b] Zanhong Deng,[b,d] Meng Li,[b,d] Shimao Wang,[b,d] Mengxiao Chen *[a,c] and Gang Meng *[b,d]

Metal oxide semiconductor (MOS)-based chemiresistors have been widely used for detecting harmful gases in many industrial and indoor/outdoor applications, which possess the advantages of small size, low cost, integratability, and ease of use. However, power consumption has become a critical parameter for practical applications. Several methods have been explored to reduce power consumption including reducing the operation temperature, use of micro-electro-mechanical systems (MEMS), and self-heating working mode. Among them, the self-heating working mode has attracted significant attention. Herein, a facile approach of modulating bridged NW chemiresistor by Joule heating effect is proposed to combine both the superiority of single crystal nanowire (NW) carrier channels and power consumption optimization of the self-heating mode. The WO_3-bridged NW chemiresistors and WO_3 film NW chemiresistors are both constructed to investigate gas responses and power consumption. Substantially magnified electrical responses (R_g/R_a) of WO_3 NW chemiresistor toward NO_2 is demonstrated by constructing a bridged structure. Under the optimal external heating condition, the responses of chemiresistors toward 5 ppm NO_2 can be boosted from 369.7 (film NW) to 1089.7 (bridged NW). The responses to 5 ppm NO_2 under the self-heating mode also can be boosted from 13.6 (film NW) to 24.6 (bridged NW) with a drastically declined power consumption. Self-heating bridged NWs allows for localizing the Joule heat within the nanojunction, and thus substantially lowers the power consumption to 0.13 μW (300 °C). This provides an additional opportunity for reducing power consumption of oxide chemiresistors for air quality monitoring in future.

Received 27th September 2022,
Accepted 19th December 2022

DOI: 10.1039/d2nr05324a

rsc.li/nanoscale

Introduction

Owing to their high responsivity, small size, low cost, low power consumption, integrability, and ease of use, metal oxide semiconductor (MOS) chemiresistors have been regarded as a promising strategy for detecting harmful gases in many industrial and indoor/outdoor applications.[1–4] Several methods have been developed to improve the sensitivity, selectivity, and stability of the chemiresistors such as noble metal modification,[5] heterojunction construction,[6] and defect regulation[7] based on traditional external heating. External heating enhances the charge exchange between the analyte gas molecules and MOS and offers sufficient activation energy until the optimal operation temperature is reached.[8–10] However, most of the MOS chemiresistors operate at a high temperature of 100–300 °C,[11] suffer from the aggregation of nanoparticles, and result in the instability of the chemiresistors.[2] The high operation temperature also limits its mobile and wireless applications. To reduce the high operation temperature and power consumption, micro-electro-mechanical systems (MEMS)[12] with small and suspended heating and sensing layer have been applied in chemiresistors.[13–15] Li *et al.*[16] reported MEMS-based Ag-modified 3D reduced graphene oxide chemiresistor, which can reduce power consumption to 52.8 mW at an operation temperature of 133 °C. Besides, the WO_3-MEMS chemiresistor has been prepared with a lower average power consumption of 15.8 mW at 250 °C compared with the general ceramic based chemiresistor of 215 mW at 250 °C in our previous work.[10] Both the shrinking of the MEMS heater volume of μm^3 compared with a general heater of several mm^3 and

[a]*Research Center for Humanoid Sensing, Zhejiang Lab, Hangzhou 311100, China. E-mail: mengxiaochen@zju.edu.cn*
[b]*Anhui Provincial Key Laboratory of Photonic Devices and Materials, Anhui Institute of Optics and Fine Mechanics, and Key Lab of Photovoltaic and Energy Conservation Materials, Chinese Academy of Sciences, Hefei 230031, China. E-mail: menggang@aiofm.ac.cn*
[c]*College of Biomedical Engineering & Instrument Science, Zhejiang University, Hangzhou 311100, China*
[d]*Advanced Laser Technology Laboratory of Anhui Province, Hefei 230037, China*
†Electronic supplementary information (ESI) available. See DOI: https://doi.org/10.1039/d2nr05324a

heater material selections contribute to a significant decrease in power consumption. Moreover, there are still several drawbacks that restrict its development, such as complicated preparation process, agglomeration problems caused by prolonged heating, and poor adhesion.[17] Utilizing the Joule heat of the sensing layer under a relatively high driven voltage (power), self-heating has demonstrated its potential in reducing the power consumption from tens of milliwatts to several microwatts by significantly reducing the heating zone to the sensing layer[18,19] (most of the power is consumed by the insulative substrate between the heater and the sensing layer for external heating including MEMS hotplate). Nanowires are ideal candidates for self-heating because of their unique quasi-one-dimensional geometric properties, which are not only beneficial for molecule sensing but also offer a robust (single crystalline) and efficient (nanowires possesses much smaller thermal conductivity than their bulk counterpart) self-heating channel. Meng *et al.*[20] reported that the suspension structure of single SnO_2 NW devices effectively blocks the dissipation of Joule heat to the substrate and achieves a high local temperature of 250 °C under the low power consumption of ~13 μW. Although single suspended NW device provides a solution to reduce chemiresistor power consumption, it still has the disadvantages of expensive preparation equipment and the low yield of device preparation. Until now, the on-chip growth of NWs network has overcome the difficulties of single NW on device preparation and also possesses outstanding properties on power consumption.[21–23] Zhu *et al.*[24] prepared a hydrogen gas sensor based on Pt-coated $W_{18}O_{49}$ nanowire networks, which could be modulated by the self-heating effect of the nanowires and possessed a comparable power level of 30–60 mW with the MEMS process.

Herein, we developed a novel self-heating on-chip bridged WO_3 NWs network for NO_2 gas sensing. We investigated the responses (R_g/R_a) of both bridged NWs and film NWs under external heating mode and self-heating mode toward various gases including NO_2, SO_2, TMA, toluene, and acetone. The bridged NW chemiresistor (0.13 μW) possesses a better gas response toward NO_2 and lower power consumption in the self-heating mode compared with film NW chemiresistor (26 μW), revealing nearly a two-order decline in power consumption. The proposed bridged NW chemiresistor achieved comparable or even better performance to the state-of-the-art MEMS and self-heating-based chemiresistors. Power consumption decline can be ascribed to the suspension structure of the bridged NWs, which can form a stable conductive channel and is conducive to localize the Joule heat generated by self-heating in the nanojunction.

Experimental section

Synthesis and characterization of bridged WO_3 NW chemiresistor

Synthesis of bridged WO_3 nanowires. Bridged WO_3 NWs were prepared by the thermal evaporation of WO_3 nanoparticles[10] and the thermal oxidation of the W film. The interdigital electrode was prefabricated on the quartz and ceramic glass substrates (Hua Chuang Rui Ke Technology Co., Ltd). Followed by sequential ultrasonic bath cleaning (ethanol, deionized water) and oxygen plasma processing (150 W, 100 Pa, 5 min), the substrates were well prepared. With a square copper mesh (Table S1, ESI†) working as a mask, the array patterned W films were then deposited on the electrode layer through radio frequency (RF) magnetron sputtering (99.95% W target, Zhongnuo New Material Technology Co., Ltd). The substrates were loaded into the sputter chamber and evacuated to a base pressure of 6×10^{-4} Pa. High purity Ar (99.999%) was then introduced into the chamber to adjust the chamber pressure to 2 Pa. Sputtering was performed at room temperature at an RF power of 100 W; the sputtering time was fixed at 30 min, allowing to obtain a patterned W film with a thickness of ~450 nm.

The as-prepared WO_3 nanoparticles (~2 mg) and patterned W film (~3 mm × 3 mm) were placed on the center and the side (~12 cm distance from the center) of the vacuum tube furnace; the average leaking rate was less than ~0.02 sccm. The evacuation of the tube chamber was stopped when it reached a base pressure of ~1 Pa. Then, the tube furnace was heated to 850 °C at a ramping rate of about 15 °C min^{-1}. The base pressure would increase rapidly at the beginning of heating and then increase slowly. After growth for 3 h, the furnace was naturally cooled toambient temperature; the dark-blue bridged $W_{18}O_{49}$ NWs were found on the patterned W film. The dark-blue bridged $W_{18}O_{49}$ NWs were changed to the yellow bridged WO_3 NWs by oxidation in air at 500 °C for 3 h. The preparation of the WO_3 NWs film chemiresistor is similar to the preparation of the bridged WO_3 NW chemiresistor except for using a square copper mesh as a mask. All of the purchased chemicals were analytical grade and used without further purification.

Characterization. The morphologies were observed by scanning electron microscopy (SEM, VGA3SBH) and optical microscopy (BX51M, OLYMPUS).

WO_3 chemiresistor self-heating and external heating tests

Both self-heating and external heating sensing performance were measured in a homemade dynamic measurement system[7] (Fig. S1, ESI†). The WO_3 NW chemiresistors were placed on a mini-stage probe station (KT-2165M4RT, Zhengzhou Ketan Instrument Equipment Co., Ltd), in which the external heating stage temperature and self-heating voltage could be well-controlled. For gas sensing tests, dry air was used as a reference gas, and diverse analytes, including SO_2, acetone, trimethylamine (TMA), toluene, and NO_2 vapors, were measured. The concentration of the analyte was tuned by diluting the standard gases with dry air with the assistance of mass flow controllers (MFC). The total flow rate of analyte gas and dry air was fixed to be 1000 sccm during measurement. The external heating temperature was controlled by the heater of mini-stage probe station. The self-heating voltage and chemiresistor resistance in air and target vapors were both controlled

and recorded by a Keithley 4200A-SCS parameter analyzer. The chemiresistor response is defined as R_g/R_a for oxidizing gases such as SO_2 and NO_2, and R_a/R_g for reducing gases such as TMA, toluene, and acetone, respectively, where R_a and R_g represent device resistance in air and the target analyte, respectively.

Results and discussion

The bridged WO_3 NW chemiresistor was fabricated through the thermal evaporation of WO_3 nanoparticles and thermal oxidation of patterned W film with the assistance of a square copper mesh (Table S1, ESI†). As shown by the schematic in Fig. 1a and b, the Pt interdigital electrode was prefabricated on the bulky ceramic substrate, and an array patterned WO_3 film layer was obtained through the thermal oxidation of array patterned W film prepared by the RF magnetron sputtering of the W target with copper mesh as a mask. Then, the bridged WO_3 NWs were grown on the film with the bottom confined by the patterned area and bridge structures formed above the interval area. The root of these NWs formed a stable contact with the WO_3 film, thus leading to a steady electrical connection with the interdigital electrode layer. Owing to the patterned structure, there is no continuous electrical circuit below the film, resulting in the charge carriers being only conducted through the "interdigital electrode-bridged NW-interdigital electrode" to form a stable conductive channel, which is clearly illustrated in Fig. 1c. Fig. 1d and e further demonstrated the detailed morphology of the whole device and the bridged NWs. In addition, the WO_3 film NW chemiresistors were also prepared by the thermal oxidation of the continuous W film (Fig. 1f, g and ESI Fig. S2†).

To examine the gas sensing performance of the proposed WO_3 NW chemiresistor, the NO_2 gas sensing test under external heating mode was carried out first. Both bridged WO_3 NW chemiresistor and WO_3 film NW chemiresistor were carefully measured under different working temperatures and NO_2 concentrations. Fig. 2a and b demonstrate the 5 ppm NO_2 gas sensing performance of bridged WO_3 NW chemiresistor and WO_3 film NW chemiresistor in the temperature range from 50 to 300 °C. The resistance increase upon exposure to oxidizing NO_2 agrees well with the n-type response characteristics of WO_3. Both responses (R_g/R_a) of the two chemiresistors toward NO_2 are noticeably improved by raising the operation temperature in the range from 50 to 200 °C (Fig. 2c), which suggests that the main surface reactive oxygen species (ROS)[25] are O^- at high temperature, and the adsorption and desorption of gas molecules reach equilibrium at the optimal operation temperature of 200 °C. Besides, the 5 ppm NO_2 response of bridged WO_3 NW chemiresistor is 1089.7, which is higher than that of the film NW chemiresistor of 369.7. The enhancement of NO_2 response characteristics can be ascribed to the specific device configuration of the bridged NW chemiresistors (Fig. 1). Firstly, in comparison with the film NW chemiresistors, the adsorption of the target molecules on the bridged WO_3 NWs would produce gate-all-around effects[26,27] on the single-crystalline NWs sensing channel, which offers a highly sensitive channel with a high utility factor. Secondly, the base resistance of the bridged WO_3 NWs is higher than that of the film NWs (Fig. 2a and b) at the same external heating temperature due to the absence of continuous W film and the well-controlled

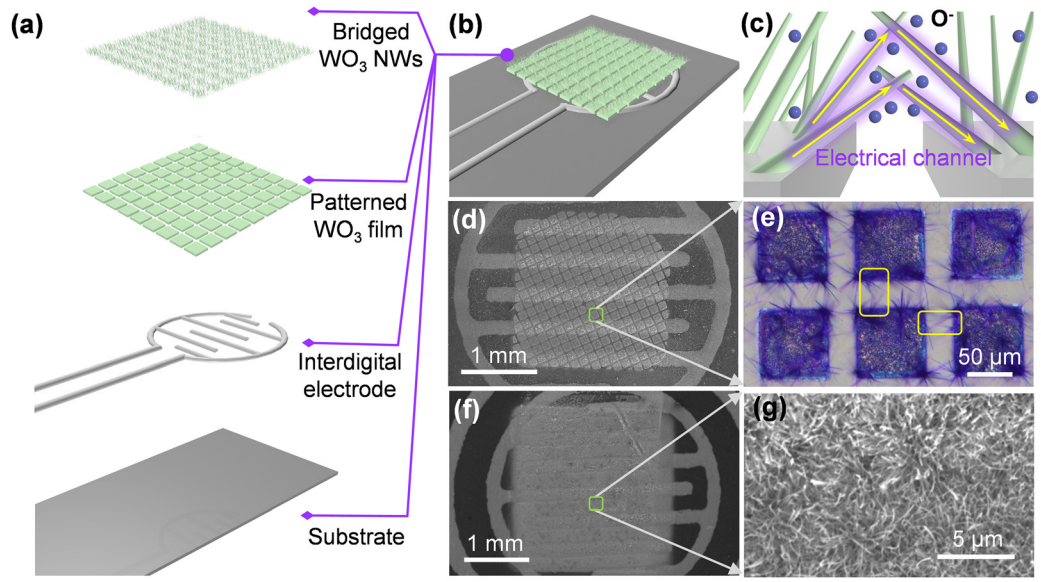

Fig. 1 Structural illustration of the integrated bridged WO_3 NW chemiresistor. (a and b) Schematic diagram of the bridged WO_3 NW chemiresistor. The NWs on the neighbouring elements are cross contacted to form a continuous electric channel when applying voltage on the interdigital electrodes. (c) Schematic diagram of the nanojunction of bridged WO_3 NW chemiresistor. The gas analyte molecules can be absorbed on the surface of bridged NWs at 360° and generate "gate-all-around" effects. (d and e) The corresponding SEM image and optical photograph of (b) and (c). (f and g) The SEM images of the WO_3 film NW chemiresistor.

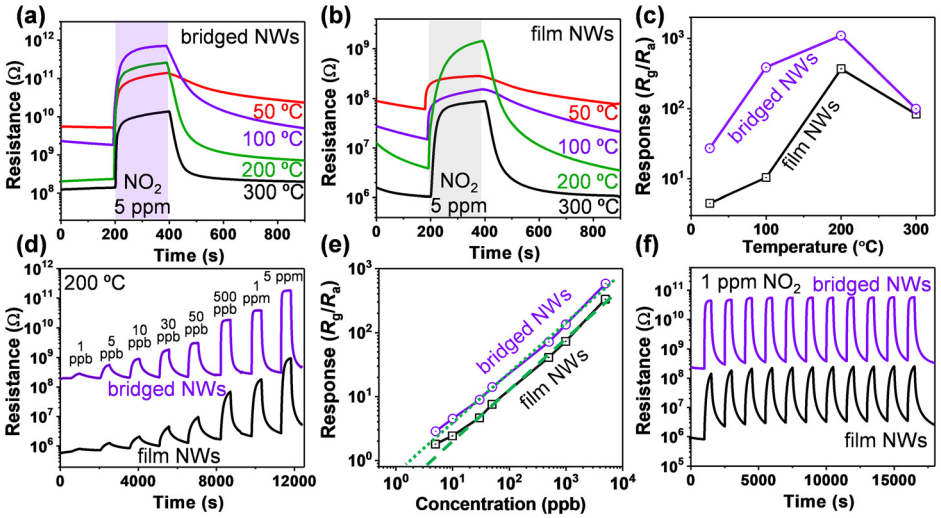

Fig. 2 The gas responses of WO_3-bridged NW chemiresistor and film NW chemiresistor toward NO_2 under external heating mode. (a and b) Resistance responses of WO_3-bridged NW chemiresistor and film NW chemiresistor to 5 ppm NO_2 molecules at different external working temperatures. The bridged NWs device possesses a higher base resistance compared with the film NWs device. The resistance decreases when the temperature increases, which agrees well with the MOS characteristics. (c) Extracted responses *versus* external working temperatures, which clearly indicates the better gas responses of WO_3-bridged NW chemiresistor than film NW chemiresistor, and the optimal operation temperature is 200 °C. (d) NO_2 concentration responses of WO_3-bridged NW chemiresistor and film NW chemiresistor under 200 °C. (e) Extracted responses *versus* NO_2 concentrations, both LoD of the WO_3-bridged NW chemiresistor and film NW chemiresistor are as low as 5 ppb. (f) Repeatability of the two chemiresistors to 1 ppm NO_2 at 200 °C.

spacing of the patterned WO_3 film. The resistance (R) is inversely proportional to the carrier concentration n, and the response is mainly dependent on the variation in the carrier concentration, which can be defined as:[27]

$$R_g/R_a = n_a/(n_a - \Delta n) \quad (1)$$

where $\Delta n = n_a - n_g$, n_a in air and n_g in target gas. A lower n_a (higher R_a) results in a higher response when a specific number of redox events (Δn) is given. The dynamic response to varying concentrations of NO_2 (Fig. 2d) indicates that the limit of detection (LoD) of the bridged WO_3 NW chemiresistor at 200 °C is approximately 5 ppb (R_g/R_a = 2.84), which is much lower than the 1-hour time-weighted average (TWA) of the recommended exposure limit (REL) of 127 ppb issued by China (GB/T 18883-2002). For 5 ppm NO_2, the response of the bridged WO_3 NW chemiresistor is 2.95 times as high as that of the film NW chemiresistor (Fig. 2e). In addition to electrical response and LoD, the device repeatability is also an important parameter for a chemiresistor. Multicycle dynamic responses of bridged WO_3 NW chemiresistor and WO_3 film NW chemiresistor toward 1 ppm NO_2 (Fig. 2f) have been carried out. The present bridged WO_3 NW chemiresistor exhibits excellent repeatability during multicycle external heating operation, which is highly required for real monitoring applications.

External heating chemiresistors possess a higher gas response; however, the drawback in power consumption limits its possible application in portable monitoring electronics. To further improve the chemiresistor performance in power consumption, the self-heating mode was adopted. Detailed characteristics of WO_3-bridged NW chemiresistor and WO_3 film NW chemiresistor under self-heating mode are described in Fig. 3. As Fig. 3a illustrates, the NWs grew on the patterned W film seed layer; part of the NW arrays grew on the interdigitated electrodes and formed stable electrical contact. There is no continuous WO_3 film between the interdigitated electrodes. The bridged NW chemiresistor conducts carriers through "interdigitated electrode-bridged NW-interdigitated electrode"; the schematic diagram of the conductive channel is shown in Fig. 3a. The self-heating responses of bridged WO_3 NWs to 5 ppm NO_2 were obtained by applying different voltages at both ends of the chemiresistor, as shown in Fig. 3b. With the increase in the driving voltage at both ends of the chemiresistor, the baseline resistance of the chemiresistor in air drops sharply, indicating that the self-heating effect begins to be obvious and the chemiresistor temperature begins to rise gradually (the resistance of the semiconductor devices decreases with the increase in temperature). At the same time, the response sensitivity of NO_2 also gradually increased and the recovery rate of the device accelerated, indicating that the Joule heat generated under high driving voltage can significantly increase the operation temperature of the chemiresistor and improve the response sensitivity and response/recovery rate when the chemiresistor does not use an external heater. The resistance of the bridged WO_3 NWs in air under different external heating temperatures and self-heating voltage is shown in Fig. 3c. The actual temperature on the nanojunction of the NWs is difficult to be measured due to the restriction of the heating conditions, which can be estimated by comparing the change in the resistance in air between self-heating and

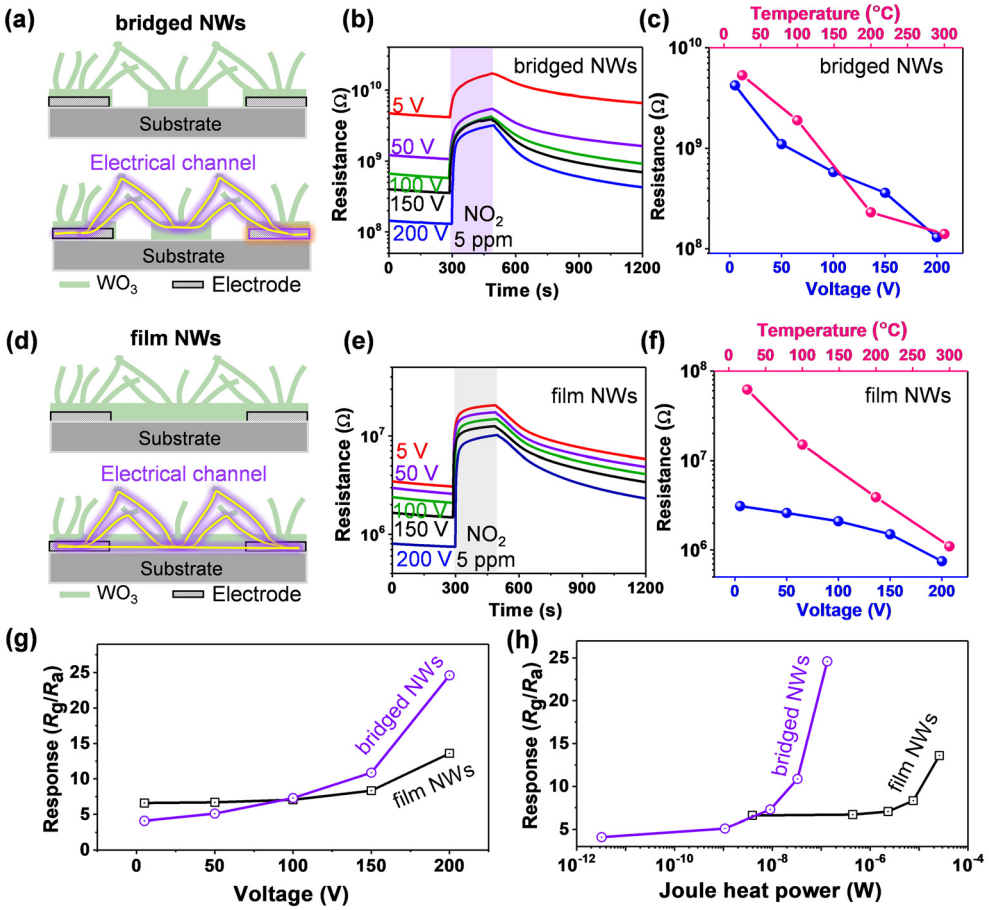

Fig. 3 The gas responses of bridged WO_3 NWs and film NW chemiresistors toward NO_2 under self-heating mode. (a) The cross-sectional schematic diagram of the bridged WO_3 NWs device and its electric channel under the self-heating mode. (b) Resistance responses of WO_3-bridged NW chemiresistors to 5 ppm NO_2 molecules under different self-heating voltages. (c) The resistance changes of bridged WO_3 NW chemiresistors under different external heating temperature and self-heating voltage. The similar resistance reduction amplitudes with increasing external heating temperature and self-heating voltage indicate that the bridged NWs produce enough Joule heat at the nanojunction under the self-heating mode. (d–f) The corresponding cross-sectional schematic diagram, resistance responses, and resistance changes at different external heating temperatures and self-heating voltage of the film NW chemiresistor, respectively. The different resistance decrease trend suggested the unobvious self-heating effect of the film NW chemiresistor. (g) The comparison of the two kinds of chemiresistors under different self-heating voltages to 5 ppm NO_2, which reveals the higher responses of bridged NW chemiresistor than the film NW chemiresistor with increasing voltage. (h) The Joule heat power comparison of the two kind chemiresistors to 5 ppm NO_2 under the self-heating mode, indicating that the lower power consumption of the self-heating bridged NW chemiresistor than the film NWs is as low as 3.3 pW at a voltage of 5 V.

external heating (known temperature) (MOS chemiresistor is similar to the thermistor, resistance is a function of temperature; therefore, the temperature can be measured by calibrating the resistance-temperature relationship). The local temperature of the bridged WO_3 NW chemiresistor is estimated to be 300 °C at a self-heating voltage of 200 V. The reduction amplitude of self-heating resistance and external heating resistance is similar, consistent with the intrinsic resistance-temperature characteristics of the chemiresistor, indicating that the bridged NWs itself can generate enough Joule heat to achieve the purpose of increasing the local temperature and reducing the heating power consumption of the chemiresistor by increasing the voltage. As a comparison, the film NW chemiresistor was prepared using the continuous W film as the seed layer. After the gas phase transport and growth of NWs, the W film was thermally oxidized to form a continuous WO_3 film. The interdigitated electrode directly contacts the continuous WO_3 NWs to form a conductive channel, as shown in Fig. 3d. The carrier was mainly transferred by the continuous WO_3 film rather than the means of "interdigitated electrode-bridged NW-interdigitated electrode". The self-heating responses of the WO_3 film NWs to 5 ppm NO_2 are shown in Fig. 3e. The baseline resistance of the WO_3 film NW chemiresistor is 2 to 3 orders of magnitude lower than that of the bridged WO_3 NWs due to the formation of carriers at the bottom of the conduction layer induced by the continuous W film seed layer. With the increase in the driving voltage at both ends of the chemiresistors, the baseline resistance of film

NWs in air decreased and the response sensitivity of NO_2 improved, showing that the film NW chemiresistor can also work in the self-heating mode. However, the effect of self-heating is significantly lower than that of the bridged WO_3 NWs. The different linear trends of the resistance at different self-heating voltages and external heating temperatures in Fig. 3f also confirmed the low effect of self-heating on the WO_3 film NWs. Fig. 3g and h show the sensitivity of bridged WO_3 NWs and WO_3 film NWs to 5 ppm NO_2 under different bias voltages and self-heating power consumption, respectively. The sensitivity of the two chemiresistors increases with the increase in self-heating power consumption. At an applied voltage of 200 V, the bridged WO_3 NW chemiresistor possesses a lower self-heating power consumption of 0.13 μW and a higher sensitivity of 24.6 compared with the WO_3 film NW chemiresistor of 26 μW and 13.6. The decrease in the self-heating voltage (5 V) leads to a lower self-heating power consumption of 3.3 pW, and the gas sensitivity to 5 ppm NO_2 is about 4.1.

Fig. 2 and 3 confirmed the higher gas sensitivity and lower self-heating power consumption of WO_3-bridged NW chemiresistor compared with the film NW chemiresistor. To present the high performance of the WO_3-bridged NWs comprehensively, we make a related comparison of gas sensitivity and power consumption, as shown in Fig. 4. Together with the NO_2 responses data shown in Fig. 2 and 3, a comparison of the optimal electrical response acquired by self-heating and external heating to 100 ppm SO_2, 100 ppm TMA, 500 ppm acetone, 500 ppm toluene, and 5 ppm NO_2 is shown in Fig. 4a. Under both self-heating and external heating modes, the bridged NW chemiresistor possesses a better selectivity toward NO_2 among various gases (Fig. S3, ESI†). Also, the gas responses under the self-heating mode would be lower than that under the external heating mode due to the limited active sites induced by the local heating area. In spite of this, the response/recovery characteristics of bridged NWs and film NW chemiresistors under different heating modes are not affected (Fig. S4, ESI†).

Fig. 4b compares the power consumption of the bridged WO_3 NW chemiresistor for NO_2 detection under self-heating mode with the state-of-the-art NO_2 chemiresistors, especially operated under the self-heating mode or MEMS-type chemiresistors. Obviously, the presented bridged WO_3 NW chemiresistor operating under the self-heating mode enabled a lower power consumption than most other chemiresistors operated in the self-heating mode or MEMS-type chemiresistors. The detailed information (sensing material, heating mode, heating temperature, power consumption, sensitivity, *etc.*) are listed in Table S2 (ESI).† Fig. 4c compares the present bridged WO_3 NW chemiresistor with the state-of-the-art WO_3-based chemiresistors operated in the external heating mode, especially sensitized by aliovalent doping, noble metal nanoparticle decoration, morphological engineering, or forming heterojunctions. Distinctly, the presented bridged NWs structure enables com-

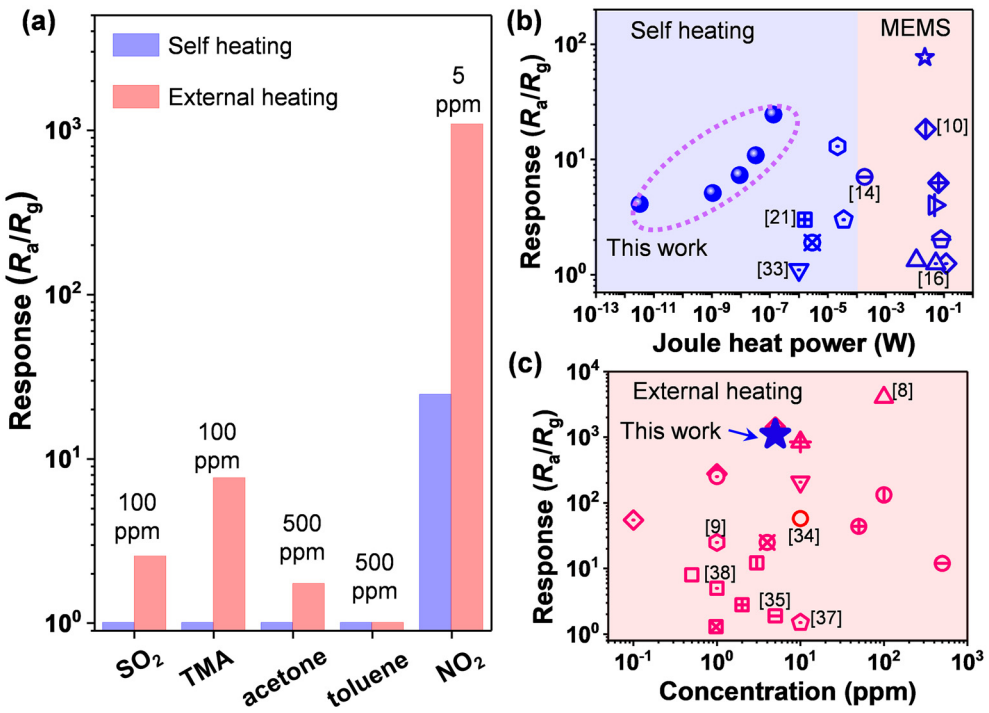

Fig. 4 (a) Histogram of bridged WO_3 NW chemiresistor electrical responses toward diverse gas molecules operated under different heating modes. (b) Joule heat power comparisons of our work (dashed line) with the reported self-heating chemiresistors and traditional external heating MEMS chemiresistors. Our work shows an ultralow power consumption compared with NO_2 chemiresistors based on the self-heating mode or MEMS-type chemiresistors. (c) NO_2 response comparisons of our work with the reported external heating devices, which possessed a comparable or even higher responses toward oxidizing NO_2 vapors than most of the existing chemiresistors.

parable or even higher responses toward oxidizing NO_2 vapors than most other chemiresistors. The detailed information (sensing material, operation temperature, device type, response/recovery time, *etc*.) are listed in Table S3 (ESI).† The WO_3-bridged NW chemiresistor possesses a better gas sensing performance compared with the WO_3 film NW chemiresistor under external heating mode and self-heating mode.

For a better understanding of the working mechanism of the bridged NW chemiresistor, Fig. 5a demonstrates the schematic diagram of external heating and self-heating for bridged WO_3 NWs, and the gas sensing mechanism between oxidized gas NO_2 and WO_3 NWs. An individual heater is necessary for the external heating mode to satisfy the temperature of the whole device. The resistance of the heater is about tens of Ohm and the heating area is more than mm^2 level, resulting in a higher heating power consumption (mW).[28–30] For the self-heating mode, the Joule heat is generated by applying a voltage at the ends of the interdigital electrode and is located at the nanojunction of bridged NWs. The Joule heat effect arises from the loss of kinetic energy in the current-carrying electrons through unavoidable collisions among themselves and with the lattice atoms, increasing with the increase in the applied voltage.[31] Therefore, the resistance sources of Joule heat in the bridged WO_3 NWs can be suggested as loss of kinetic energy (collision of electrons with one another and with W^{6+} and O^{2-} ions) of electrons in the WO_3 grains, WO_3 grain boundaries, and WO_3–WO_3 homojunction.[32] The higher the resistance, the higher the Joule heat.[33] According to the equation $P = U^2/R$ (P: power consumption, U: voltage), the resistance is inversely proportional to power consumption. The higher the resistance, the lower the power consumption. The resistance of the bridged WO_3 NWs is much larger than that of the external heater, resulting in ultralow power consumption, as shown in Fig. 5b. Besides, the suspension structure effectively blocks the Joule heat dissipation/conduction from the (tip) bridged nanowires to the (bottom) substrate and offers an extremely high utilization efficiency of Joule heat compared with the film NWs device, resulting in ultralow power consumption. Fig. 5c and d show the schematic illustration of the gas molecules absorbed on the bridged WO_3 NWs. When the chemiresistor is exposed to air, the O_2 molecules can adsorb on the surface of n-type WO_3 NWs, capture free electrons from the adsorption sites on the oxide surface, and generate ROS (O_2^- and O^-), as shown in the following equations.[34–36]

$$O_{2(gas)} \leftrightarrow O_{2(ads)} \quad (1)$$

$$O_{2(ads)} + e^- \leftrightarrow {O_2}^-_{(ads)} \ (\text{RT to } 150^\circ\text{C}) \quad (2)$$

$${O_2}^-_{(ads)} + e^- \leftrightarrow 2{O}^-_{(ads)} \ (\sim 150^\circ\text{C to} \sim 300^\circ\text{C}) \quad (3)$$

The adsorption of O_2 would induce a thin electron depletion layer (EDL) on the surface of the sensing material and lead to a slight elevation of the device resistance (R_0) (Fig. 5c and d). When exposed to NO_2, NO_2 would not only

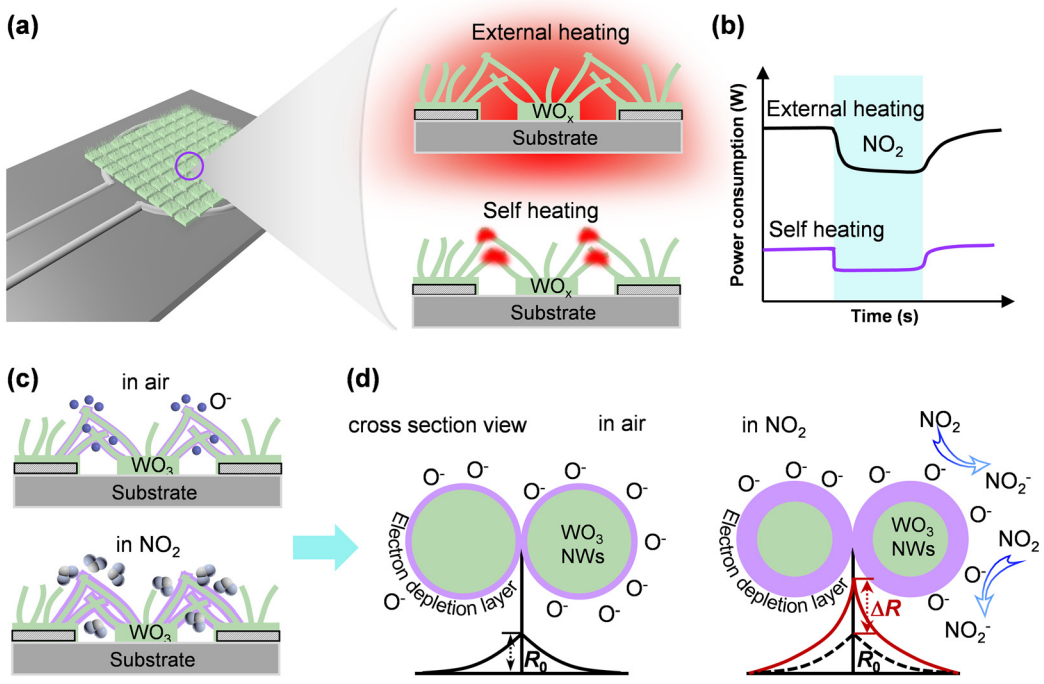

Fig. 5 Sensing mechanism of bridged WO_3 NW chemiresistor. (a and b) Schematic illustration of the produced Joule heat, explaining the lower power consumption of self-heating of bridged NW chemiresistor compared with the external heating mode. (c and d) Schematic illustration of the interaction process between the analyte gas molecules and the WO_3 NWs surface under the self-heating mode. The exposure in NO_2 increases with the thickness in the electron depletion layer (EDL) and the increase in the chemiresistor resistance (ΔR).

capture free electrons from the surface of WO_3 NWs but also react with ROS, as shown below.[37,38]

$$NO_{2(gas)} + e^- \rightarrow NO_2{}^-{}_{(ads)} \quad (4)$$

$$NO_{2(gas)} + O_2{}^-{}_{(ads)} + 2e^- \rightarrow NO_2{}^-{}_{(ads)} + 2O^-{}_{(ads)} \quad (5)$$

$$NO_2{}^-{}_{(ads)} + O^-{}_{(ads)} + 2e^- \rightarrow NO_{(gas)} + 2O^{2-}{}_{(ads)} \quad (6)$$

The width of the EDL further increases, leading to a higher resistance of WO_3 NWs ($R_0 + \Delta R$) (Fig. 5d).

Conclusion

In this work, a strategy combining bridged NWs construction with self-heating operation mode was proposed to address the bottleneck issue of high heating power consumption in MOS chemiresistor. The as-prepared bridged WO_3 NW chemiresistors were carefully measured under both self-heating mode and external heating mode. Compared with traditional WO_3 film NW chemiresistor, bridged WO_3 NW chemiresistor possessed higher responsibility, selectivity, and lower power consumption for various gases including NO_2, TMA, and SO_2. Under the external heating mode, the optimal response of the bridged WO_3 NW chemiresistor to 5 ppm NO_2 is 1089.7, which is 2.95 times as high as that of the WO_3 film NW chemiresistor (369.7). Under the self-heating mode, the optimal response of bridged WO_3 NW chemiresistor to 5 ppm NO_2 is 24.6, which is 1.8 times as high as that of the WO_3 film NW chemiresistor. The power consumption of the self-heating bridged WO_3 NW chemiresistor is 3.3 pW–0.13 μW under 5–200 V working voltage, while the WO_3 film NW chemiresistor needs 26 μW power consumption under 200 V. The power consumption of the self-heating WO_3-bridged NW chemiresistor is lower than most WO_3-based chemiresistors operated under external heating mode with a power consumption of several tens of milliwatts to hundreds of milliwatts. The proposed strategy of self-heating bridged MOS NWs devices will definitely enable new opportunities for MOS chemiresistors in diverse areas such as wearable gas monitoring and IoT.

Author contributions

The manuscript was written through the contributions of all authors. All authors have given approval to the final version of the manuscript.

Conflicts of interest

There are no conflicts to declare.

Acknowledgements

The authors gratefully acknowledge financial support by Research Initiation Project of Zhejiang Lab (No. 2022MG0PI01), National Natural Science Foundation of China (52202191, 62075223), the CAS Pioneer Hundred Talents Program, CAS-NSTDA Joint Research Projects (GJHZ202101), the Key Lab of Photovoltaic and Energy Conservation Materials (PECL2021QN001).

References

1 S. Choi, Y. Kim, T. Van Nguyen, W. H. Jeong, K.-S. Min and B. J. Choi, *Adv. Electron. Mater.*, 2021, **7**, 2100050.
2 T. M. Ngoc, N. Van Duy, C. M. Hung, N. D. Hoa, H. Nguyen, M. Tonezzer and N. Van Hieu, *Anal. Chim. Acta*, 2019, **1069**, 108–116.
3 C. S. Prajapati and N. Bhat, *Sens. Actuators, B*, 2018, **260**, 236–242.
4 W. Lee, H. Park, S. Y. Kim, S.-M. Park, D. H. Kim and H. Lee, *Adv. Electron. Mater.*, 2021, **7**, 2001240.
5 T. Dai, Z. Yan, M. Li, Y. Han, Z. Deng, S. Wang, R. Wang, X. Xu, L. Shi, W. Tong, J. Bao, Z. Qiao, L. Li and G. Meng, *Small Methods*, 2022, **6**, 2200728.
6 D. R. Miller, S. A. Akbar and P. A. Morris, *Sens. Actuators, B*, 2014, **204**, 250–272.
7 B. Tong, Z. Deng, B. Xu, G. Meng, J. Shao, H. Liu, T. Dai, X. Shan, W. Dong, S. Wang, S. Zhou, R. Tao and X. Fang, *ACS Appl. Mater. Interfaces*, 2018, **10**, 34727–34734.
8 T. Dai, Z. Deng, S. Wang, X. Fang and G. Meng, *Nanoscale*, 2022, **14**, 5002–5009.
9 N. Kaur, D. Zappa, V. A. Maraloiu and E. Comini, *Adv. Funct. Mater.*, 2021, **31**, 2104416.
10 T. Dai, G. Meng, Z. Deng, Y. Chen, H. Liu, L. Li, S. Wang, J. Chang, P. Xu, X. Li and X. Fang, *ACS Appl. Mater. Interfaces*, 2020, **12**, 37295–37304.
11 J.-H. Kim, A. Mirzaei, H. W. Kim and S. S. Kim, *Sens. Actuators, A*, 2020, **308**, 112011.
12 B. Yang, N. V. Myung and T.-T. Tran, *Adv. Electron. Mater.*, 2021, **7**, 2100271.
13 J.-L. Hou and T.-J. Hsueh, *ACS Appl. Electron. Mater.*, 2021, **3**, 4817–4823.
14 I. Cho, Y. C. Sim, M. Cho, Y. H. Cho and I. Park, *ACS Sens.*, 2020, **5**, 563–570.
15 I. Cho, K. Kang, D. Yang, J. Yun and I. Park, *ACS Appl. Mater. Interfaces*, 2017, **9**, 27111–27119.
16 Q. Li, D. Chen, J. Miao, S. Lin, Z. Yu, Y. Han, Z. Yang, X. Zhi, D. Cui and Z. An, *ACS Appl. Mater. Interfaces*, 2020, **12**, 25243–25252.
17 T. M. Ngoc, N. Van Duy, N. Duc Hoa, C. Manh Hung, H. Nguyen and N. Van Hieu, *Sens. Actuators, B*, 2019, **295**, 144–152.
18 J. H. Kim, A. Mirzaei, H. W. Kim and S. S. Kim, *ACS Appl. Mater. Interfaces*, 2019, **11**, 24172–24183.
19 B. Behera and S. Chandra, *Mater. Sci. Semicond. Process.*, 2018, **86**, 79–84.
20 G. Meng, F. Zhuge, K. Nagashima, A. Nakao, M. Kanai, Y. He, M. Boudot, T. Takahashi, K. Uchida and T. Yanagida, *ACS Sens.*, 2016, **1**, 997–1002.

21 S. M. Majhi, A. Mirzaei, H. W. Kim, S. S. Kim and T. W. Kim, *Nano Energy*, 2021, **79**, 105369.
22 H. M. Tan, C. Manh Hung, T. M. Ngoc, H. Nguyen, N. Duc Hoa, N. Van Duy and N. V. Hieu, *ACS Appl. Mater. Interfaces*, 2017, **9**, 6153–6162.
23 J.-H. Kim, H. W. Kim and S. S. Kim, *Sens. Actuators, B*, 2017, **251**, 781–794.
24 L. Zhu, J. She, J. Luo, S. Deng, J. Chen, X. Ji and N. Xu, *Sens. Actuators, B*, 2011, **153**, 354–360.
25 R. Zhang, Z. Deng, L. Shi, M. Kumar, J. Chang, S. Wang, X. Fang, W. Tong and G. Meng, *ACS Appl. Mater. Interfaces*, 2022, **14**, 24536–24545.
26 Y. Kang, S. Xu, K. Han, E. Y. J. Kong, Z. Song, S. Luo, A. Kumar, C. Wang, W. Fan, G. Liang and X. Gong, *Nano Lett.*, 2021, **21**, 5555–5563.
27 T. Dai, Z. Deng, X. Fang, H. Lu, Y. He, J. Chang, S. Wang, N. Zhu, L. Li and G. Meng, *Small Methods*, 2021, **5**, 2100202.
28 Y. Shen, H. Bi, T. Li, X. Zhong, X. Chen, A. Fan and D. Wei, *Appl. Surf. Sci.*, 2018, **434**, 922–931.
29 E. Rossinyol, A. Prim, E. Pellicer, J. Arbiol, F. Hernández-Ramírez, F. Peiró, A. Cornet, J. R. Morante, L. A. Solovyov, B. Tian, T. Bo and D. Zhao, *Adv. Funct. Mater.*, 2007, **17**, 1801–1806.
30 P. Thi Hong Van, N. Hoang Thanh, V. Van Quang, N. Van Duy, N. Duc Hoa and N. Van Hieu, *ACS Appl. Mater. Interfaces*, 2014, **6**, 12022–12030.
31 J.-H. Kim, A. Mirzaei, H. W. Kim and S. S. Kim, *Sens. Actuators, B*, 2018, **267**, 597–607.
32 J. Y. Kim, J. H. Lee, J. H. Kim, A. Mirzaei, H. W. Kim and S. S. Kim, *Sens. Actuators, B*, 2019, **299**, 126965.
33 T. M. Ngoc, N. Van Duy, C. M. Hung, N. D. Hoa, N. N. Trung, H. Nguyen and N. Van Hieu, *RSC Adv.*, 2018, **8**, 36323–36330.
34 N. Lu, C. Yang, P. Liu and X. Su, *J. Colloid Interface Sci.*, 2019, **557**, 311–317.
35 O. Chmela, J. Sadilek, G. Domenech-Gil, J. Sama, J. Somer, R. Mohan, A. Romano-Rodriguez, J. Hubalek and S. Vallejos, *Nanoscale*, 2018, **10**, 9087–9096.
36 J.-H. Kim, J.-H. Lee, Y. Park, J.-Y. Kim, A. Mirzaei, H. W. Kim and S. S. Kim, *Sens. Actuators, B*, 2019, **294**, 78–88.
37 K. Lee, D.-H. Baek, H. Na, J. Choi and J. Kim, *Sens. Actuators, B*, 2018, **265**, 522–528.
38 L. Yuan, M. Hu, Y. Wei and W. Ma, *Appl. Surf. Sci.*, 2016, **389**, 824–834.